Ninth International Conference on Computational Fluid Dynamics (ICCFD9), Istanbul, Turkey, July 11-15, 2016 **ICCFD9-xxxx**

An IBM-FSI solver of flexible objects in fluid flow for pumps clogging applications

A. Albadawi[1], S. Marry[2], B. Breen[2], R. Connelly[2], Y. Delaure[1]

[1] School of Mech. and Manuf. Eng., Dublin City University, Dublin9, Ireland
[2] Sulzer Pump Solutions Ireland Ltd., Wexford, Ireland

Corresponding author: abdulaleem.albadawi@dcu.ie

Abstract: A range of pumps have been developed to handle mixtures of liquid and suspended solids and rags. The increase in certain solid wastes found in municipal sewage water, however, can pose significant challenges. The rate of accumulation of rags and fibrous clumps is known to depend on the flow conditions and certain hydrodynamic properties of the pumps. While it is difficult to characterize and quantify experimentally the mechanism that leads to clogging, a fully coupled fluid and solid computational simulation would allow a visualization of the deformation of immersed suspended material, a characterization of the flow and solid dynamic behaviors and, crucially, an assessment of correlations between fluid and solid responses. Although theoretically feasible, the task is far from straightforward and no such solution has yet been published for a full pump case. This article presents initial work on a model developed specifically to study flexible cloths like structures (rags). A computational Fluid Structure Interaction (FSI) model has been developed and validated. The model includes (i) a Navier-Stokes Finite Volume solver for the flow equations, (ii) a coupling algorithm preserving the no slip boundary condition at the interface, (iii) a Finite Difference solution of the variational derivative of the deformation energy for the solid, and (iv) a solid-fluid interface tracking model. The no slip boundary condition at the solid-fluid interface is maintained by adding a momentum source term in both the solid and the fluid solvers. This solution is based on the Immersed Boundary Method (IBM) proposed in [1] which treats the rag or fiber as a Lagrangian elastic body. Both structural and fluid solvers are implemented in the open source platform OpenFOAM®. The method is mainly used in the literature to analyze the oscillational behavior of filaments or rags constrained at one end. It is extended here to account for rag/filament transport in a flowing fluid and interactions with fixed obstacles. Results are compared to published simulations for validation and then applied to a range of test cases chosen to represent conditions found in pump applications. The code has been extended for the study of cases relevant to processes leading up to rag blockage. This includes the analysis of the filament/rag motion behind an obstacle, and the interaction of the deformed object with rigid solid surfaces. The IBM solver for rag motion in fluid flow is combined with two different collision models for modeling the interaction of the deformable object with the side walls: (1) A method similar to the hard sphere collision model is considered to correct the velocity of the Lagrangian points during collision, and (2) a force based model where a short range repulsive force [2] is applied once the distance between the slender object and the solid wall becomes smaller than a specific threshold. The results are assessed qualitatively and show that the flag's response does depend on the collision model, and confirm the importance of using a force based model that can be adopted to account for the solid - solid friction or the lubrication effect.

Keywords: Immersed Boundary Method, Fluid Structure Interaction, Rag model, Pumps clogging, OpenFOAM.

1 Introduction

Fluid-Structure interaction problems (FSI) are encountered in many biological and engineering applications. Examples that can be found in the literature include insect wings [3, 4], fish-like locomotion [5, 6, 7], human heart valves [8], energy harvesting devices [9], flag oscillations [10, 11, 12], inverted flag [13]. The physics of flag motion is of particular interest to our project since it describes the rag motion in a free stream fluid flow and inside waste water pumps. Despite the difference in the flow regimes and Reynolds numbers in these applications, the deformable objects involved share the same feature involving arbitrary large deformations of the flexible bodies inside complicated geometrical fluid domains. The structure can be described as a thin membrane in a fluid flow which is either pinned or free from its sides. As the flow passes over the deformable surface and leaves at the trailing edge, an instability develops leading to sustained oscillations of the membrane. At the same time, the general motion of the deformable object leads to vortex shedding at its free ends. The fluid - solid system includes membrane motion, vortex shedding, membrane inertia effect, membrane bending rigidity restoring effect, and Reynolds number effect.

Conventional numerical approaches for solving fluid - solid interaction problems are the Arbitrary Lagrangian Eulerian formulation [14, 15] and the Immersed Boundary methods (IBM). In the former method, the fluid and solid domains are meshed separately. The boundary condition at the solid surface can be imposed in a straightforward manner. However, an algorithm should be adopted in order to move the fluid mesh in accordance with the motion of the solid object. This poses a challenging problem in terms of the computational efficiency when the solid object experiences large deformations. The Immersed Boundary methods, on the other hand, are well-suited for complex large deformation of the solid bodies. Although the IBM methods vary based on their implementation (the Continuous Forcing approach by Peskin [16], the Direct Forcing approach [17, 18], and the Projection approach [19]), they all share the same advantage which is the capability of modeling large object deformations without the need for re-meshing of the fluid domain.

The main idea of the Immersed Boundary methods to avoid the complexity of mesh conforming is by adding a momentum forcing to the equation of motion in order to mimic the complex boundaries. For the different available IBM methods, this momentum forcing can be formulated directly on the discretized grids (Discrete Forcing approach [17, 20, 21]) or it can be calculated first on the Lagrangian points representing the solid domain and then it is transferred to the Eulerian fluid domain using smoothed approximation of the Dirac delta function (Continuous Forcing approach [22, 23]). For more details about the various types of the IB methods, the reader is referred to the extensive review papers by Sotiropoulos and Yang [24] and the earlier review by Mittal and Laccarino [25]. In the present study, we focus on the momentum forcing formulation in the continuous IBM methods.

Among the early IB methods used for solving the fluid -structure coupling is the one developed by Peskin [26]. In this method, the neutrally buoyant elastic boundaries are accomplished by adding a momentum forcing to the Navier Stokes equations. This force has non zero values only near or on the structure. Kim and Peskin [27] developed the Penalty Immersed Boundary method which uses two sets of material points (massive and massless sets). The two sets are restrained together using a stiff spring. The massless points are moved according to the Eulerian fluid velocity, while the massive points are calculated in Lagrangian coordinates. To handle the mass for fluid - structure interactions, Huang et. al, 2007 [23] used a feedback forcing approach [22]. In this method, a tension force is used for controlling the constraint of the inextensibility. However, two additional large constants are introduced in the forcing momentum approach which imposes a limitation on the computational time step for solving the governing equations. This formulation has later been reformulated using the inertia term in the motion equation of the solid structure [1]. The equations of the fluid and solid domains are solved separately. To avoid the added constraint on the time step, Lee and Choi, 2015 [28] solved the governing equations using the discrete forcing approach where the momentum force used for the coupling is obtained directly from the Navier Stokes equations. The structural equation in this method is solved on Lagrangian coordinates using thin blocks segmented together to form the slender body. Pan et. al, 2014 [29] have used the pressure difference on the top and bottom of the structural object for calculating the IBM force. The structural solver in this case is based on the thin shell model. Therefore, this method requires that there is a specific thickness for the flag.

The numerical study of a filament flapping using both ALE and IBM methods has received significant interest the last decade [30, 10, 23]. These studies have concentrated on the flapping of a filament fixed from one end and free from the other end under the effect of fluid flow. Its stability has been investigated under the effect of different fluid and solid characteristics (Reynolds number, solid bending rigidity, solid to fluid mass ratio). The model has since been extended for simulating two-dimensional (2D) flag oscillation in a three-dimensional flow [11, 31, 32]. The objective of these numerical studies is to extend the understanding of the filament stability towards flag stability in a free stream. It is also worth mentioning the numerical studies which focused on the effect of the wake generated behind a cylinder on the filament oscillation [29, 33, 34]. Despite the widespread use of the IBM methods for modeling flag oscillation, there is, to the authors knowledge, a lack of study of the flag motion in free stream or behind obstacles. Furthermore, apart from the Dirac repulsive collision model used in Huang et. al, 2007 [23], there are no studies on the collision of flexible objects against solid walls. In the present work, we describe initial work towards the development of an Immersed Boundary method for the study of rag motion and interaction with solid walls inside waste water pumps. This includes the study of rag motion in a free stream and behind an obstacle. The collision of the deformable rag against solid objects is also considered. The main objective of this study is to understand the clogging process in waste water pumps. These pumps can become partially clogged when the rag wraps itself around the single impeller. This occurs when the upstream liquid flow pins the rag to the flat base of the rotor on which the impeller is mounted.

In this paper, an immersed boundary method based on [11, 23] is implemented in the Open source library OpenFOAM-2.3.1 [35]. The motion of the deformable object is developed using the variational derivative of the deformation energy [1] on a Lagrangian grid. The fluid motion is solved using the PIMPLE solver available in OpenFOAM on an Eulerian grid. The fluid - solid interaction is modeled using a momentum forcing term added to the solid equation and spread into the Eulerian frame using a Dirac function. The small time step required by this momentum forcing approach is of the same order as the time step required for modeling flow motion inside the pumps. The paper is organized as follows. In next section, the problem formulation is described. The model is then validated using both filament oscillation and flag oscillation in a free stream. The code is used for simulating free flag motion in a free stream and behind an obstacle. Finally, the collision models implemented in the code are analyzed using flag collision against side walls and rigid obstacle.

2 Problem Formulation

This section describes the three dimensional (3D) computational model for simulating the motion of elastic slender objects in fluid flow. Two different cases are recognized based on the dimensions of the solid object (Figure 1); (I) filament motion (1D) in a 2D free stream, (II) 2D flag motion in a 3D free stream.

2.1 Governing Equations

The incompressible viscous fluid flow is governed by the Navier Stokes equations written as:

$$\rho_f(\frac{\partial \mathbf{u}}{\partial t} + \mathbf{u} \cdot \nabla \mathbf{u}) = -\nabla p + \mu \nabla^2 \mathbf{u} + \mathbf{f} \tag{1}$$

$$\nabla \cdot \mathbf{u} = 0 \tag{2}$$

where ρ_f is the fluid density, $\mathbf{u}$ is the fluid velocity, p is the fluid pressure, μ is the fluid viscosity, and $\mathbf{f}$ is the momentum forcing applied to enforce the no-slip boundary condition along the interface between the flexible object and the fluid flow. The fluid is solved using the PIMPLE solver available in the open source library OpenFOAM-2.3.1 [35] where the governing equations are discretized based on a Finite Volume formulation. The fluid domain is discretized in this study on an Eulerian uniform structured mesh. The spatial derivatives are discretized using second order schemes while the time derivatives are discretized using the Euler implicit scheme. The pressure-velocity coupling is solved using the merged SIMPLE-PISO algorithm (PIMPLE) [36]. The Semi-Implicit Method for Pressure-Linked equations (SIMPLE) [37] couples the Navier-Stokes equations with an iterative procedure in order to calculate the pressure scalar values using the updated velocity, while the Pressure Implicit Splitting Operator (PISO) [38] algorithm is used to rectify the pressure-velocity correction. For more details about the fluid solver, the reader is referred to the OpenFOAM user

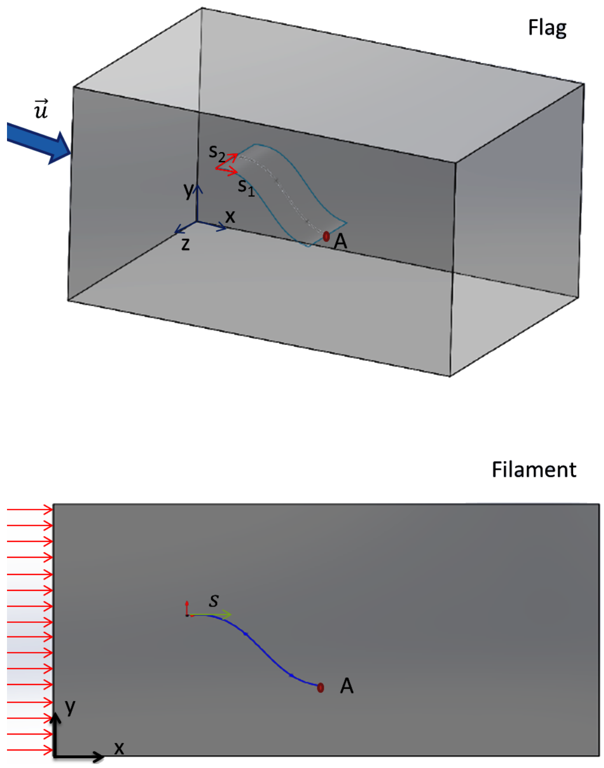

Figure 1: Schematic diagram of the computational configuration and coordinate systems; Top: 2D flag in a free stream, Bottom: 1D filament in a free stream.

guide [36].

The equation of motion of the elastic body is derived in a Lagrangian frame (s_1, s_2) using the variational derivative of the deformation energy [1]. For a flexible filament in a two dimensional flow, the governing equation for the motion of the filament can be written as:

$$\rho_1 \frac{\partial^2 \mathbf{X}}{\partial t^2} = \frac{\partial}{\partial s}(\sigma_{11} \frac{\partial \mathbf{X}}{\partial s}) - \frac{\partial^2}{\partial s^2}(\gamma_{11} \frac{\partial^2 \mathbf{X}}{\partial s^2}) + \rho_1 \mathbf{g} - \mathbf{F} + \mathbf{F}_c \tag{3}$$

where s in the arc length, $\mathbf{g}$ is the gravitational acceleration, $\mathbf{X}$ is the position vector of the Lagrangian solid points, σ_{11} is the tension force along the filament axis, γ_{11} is the bending rigidity, $\mathbf{F}$ is the momentum forcing which represents the effect of the fluid on the solid, and $\mathbf{F}_c$ is the collision force. The term ρ_1 denotes the density difference between the filament and the surrounding fluid, and it has the value $\rho_1 = 0$ for neutrally buoyant objects. Two different boundary conditions are applied for the filament case: (1) free end boundary condition ($\sigma_{11} = 0$, $\frac{\partial^2 \mathbf{X}}{\partial s^2} = (0,0)$, $\frac{\partial^3 \mathbf{X}}{\partial s^3} = (0,0)$) and (2) fixed end boundary condition ($\mathbf{X} = constant$, $\frac{\partial^2 \mathbf{X}}{\partial s^2} = (0,0)$).

For a flexible two dimensional flag in a 3D free stream, the governing equation for the motion of the flag can be written as:

$$\rho_1 \frac{\partial^2 \mathbf{X}}{\partial t^2} = \sum_{i,j=1}^{2} [\frac{\partial}{\partial s_i}(\sigma_{ij} \frac{\partial \mathbf{X}}{\partial s_j}) - \frac{\partial^2}{\partial s_i \partial s_j}(\gamma_{ij} \frac{\partial^2 \mathbf{X}}{\partial s_i \partial s_j})] + \rho_1 \mathbf{g} - \mathbf{F} + \mathbf{F}_c \tag{4}$$

where $\sigma_{ij} = \varphi_{ij}(T_{ij} - T_{ij}^0)$ and $\gamma_{ij} = \zeta_{ij}(B_{ij} - B_{ij}^0)$. The term $T_{ij} = \frac{\partial \mathbf{X}}{\partial s_i} \cdot \frac{\partial \mathbf{X}}{\partial s_j}$ refers to the stretching effect $(i = j)$ or the shearing effect $(i \neq j)$, while the term $B_{ij} = \frac{\partial^2 \mathbf{X}}{\partial s_i \partial s_j} \cdot \frac{\partial^2 \mathbf{X}}{\partial s_i \partial s_j}$ refers to the bending effect $(i = j)$ or the twisting effect $(i \neq j)$. The constants φ_{ij} and ζ_{ij} are the tension and bending coefficients, respectively. The superscript 0 denotes the initial value. The density difference ρ_1 can be calculated as $\rho_1 = \rho_s - \rho_f c$ where

ρ_s is the solid density and c is the flag thickness. Two different boundary conditions are also applied for the flag case: (1) fixed boundary ($X = constant$, $\frac{\partial^2 \mathbf{X}}{\partial s_i^2} = (0,0)$ For $i = 1$ or 2) and (2) the free end boundary ($\frac{\partial^2 \mathbf{X}}{\partial s^2} = (0,0)$, $\frac{\partial^3 \mathbf{X}}{\partial s^3} = (0,0)$ For $i = 1$ or 2 and $\sigma_{ij} = 0, \gamma_{ij} = 0$ For $i = 1$ or 2).

The equation of motion of the solid solver is discretized using the Finite Difference formulation following the approach introduced in [1, 23]. This discretization is a first order accurate and it requires small time steps to avoid instability. However, the order of the time step size used in this paper is the same as that required for solving the fluid flows inside the single impeller rotating pumps used in our application. For comparisons against the numerical benchmarking data, the following non-dimensional parameters can be defined using the flag/filament length L and the free stream velocity U: the non dimensional time $t^* = tL/U$, the non dimensional length $y^* = y/L$, Reynolds number $Re = \frac{\rho_f UL}{\mu}$, Froude number $Fr = gL/U^2$, the non-dimensional bending rigidity $K_B = \frac{\zeta}{\rho_1 U^2 L^2}$, the non-dimensional tension coefficient $K_T = \frac{\varphi}{\rho_1 U^2}$, and the non-dimensional mass ratio $\rho = \frac{\rho_1}{\rho_f L}$. For the rest of the paper, the non dimensional values are considered and the Astrix is dropped from the non dimensional time and length values.

2.2 Fluid - Structure Interaction

The momentum forcing term employed by [11, 1] is adopted in this paper to deal with the fluid - solid interaction. This force is evaluated directly from the equation of solid motion. Two sets of Lagrangian points are used: The structure points (X) calculated from the flag motion equation and the immersed boundary points (X_{ib}) obtained from local fluid velocity U_{ib}. The momentum forcing in the solid equation is calculated as:

$$\mathbf{F} = -K_{ibm}(\mathbf{X}_{ib}^{n+1} - 2\mathbf{X}^n + \mathbf{X}^{n-1}) \tag{5}$$

where the superscript n represents the time step, $\mathbf{X}_{ib}^{n+1}$ is the new estimated position of the IB point and is calculated as $\mathbf{X}_{ib}^{n+1} = \mathbf{X}_{ib}^n + \mathbf{U}_{ib}^n \Delta t$. The velocity $\mathbf{U}_{ib}^n$ at the position $\mathbf{X}_{ib}^n$ is calculated by linearly interpolating the velocity value at the closest cell center on the Eulerain frame. K_{ibm} is a large constant value [1]. The Lagrangian momentum forcing is spread into the Eulerian domain by using the Dirac delta function as:

$$\mathbf{f}^n = \int_\Gamma \mathbf{F}^n(\Gamma, t)\delta(\mathbf{x} - \mathbf{X}^n(\Gamma, t))d\Gamma \tag{6}$$

Note that the integration is $\int_\Gamma (-)d\Gamma = \int_s (-)ds$ for the filament case and $\int_\Gamma (-)d\Gamma = \int_{s_1}\int_{s_2} (-)ds_1 ds_2$ for the flag case. The Dirac function for moving flags in a 3D fluid flow is calculated using four points as:

$$\delta(\mathbf{X}) = \frac{1}{h^3}\varphi(\frac{x}{h})\varphi(\frac{y}{h})\varphi(\frac{z}{h}) \tag{7}$$

$$\varphi(r) = \begin{cases} \frac{1}{8}(3 - 2|r| + \sqrt{1 + 4|r| - 4|r^2|}) & 0 \le |r| < 1 \\ \frac{1}{8}(5 - 2|r| + \sqrt{-7 + 12|r| - 4|r^2|}) & 1 \le |r| < 2 \\ 0 & 2 \le |r| \end{cases} \tag{8}$$

where h is the Eulerian mesh size. For non-dimensional solvers, the Eulerian momentum forcing is multiplied by the mass ratio ρ for non-dimensionalisation purposes.

2.3 Collision Model

In this paper, we present a model for collision of deformable objects with solid surfaces. The accurate modeling of collision can be challenging due to multiple effects taking place. These include the large surface deformation, the squeezing of the liquid trapped between the two colliding objects, the excessive local grid refinement which would ideally be required to resolve the liquid film, and the physical properties of both the colliding objects and the fluid domain. To the authors knowledge, most published research to date has focused on either the collision of two rigid objects (Lubrication theory) or the collision of small particles against rigid walls. However, for the collision between two oscillating flexible filaments, Huang et. al, 2007 [23] has incorporated a collision model into the filament solid equation based on a repulsive force calculated using the Dirac delta function in the line connecting the two colliding points of the approaching filaments but this did not take account of dominant forces from fluid structure interactions.

Contrary to the collision of the deformable objects against rigid walls, various approaches have been considered for particle-wall collision, (a) the mesh between the two colliding objects may be reduced sufficiently so that the collision process can be modeled with the traditional Navier Stokes equations, (b) hard sphere model where a solid body collision model may be implemented whereas the position of the colliding objects is modified if the collision takes place after solving the momentum equation of these objects [39, 40], (c) soft sphere model which applies normal and tangential forces to the momentum equation of the colliding objects using the overlapping distance between them [41, 42], (d) short range repulsive force is implemented once the distance between the two objects goes below a specific threshold [2, 43], (e) repulsive force based on the lubrication theory is implemented once the distance between the two objects falls below a specific value [44], (f) coupled model considering both a repulsive force and a lubrication force [45, 46]. A review of the different collision models is available in [45].

In the present study, two different approaches are considered: (a) A correction similar to the hard sphere model is implemented where the position of the Lagrangian points is updated using only the effect of fluid flow. Upon solving the momentum equation of the flexible object, the position of the Lagrangian points are corrected using this model if the normal distance between this point and closest rigid surface falls below a specific threshold from the rigid surface or if the Lagrangian point penetrates the rigid surface.

$$\mathbf{X}^{n+1} = \mathbf{X}^{n} + \mathbf{U}_{ib}^{n} \times \Delta t \tag{9}$$

The second model implements a short range repulsive force for handling the collision between the deformable objects and the solid surfaces. Due to the fluid lubrication (water in the case of waste water pumps), there is no contact during the collision process. Rather, the two objects interact repulsively via the intervening liquid when they are in a close proximity. In the present simulations, the repulsive force is activated once the distance between the colliding objects falls below a specific threshold ($2h$). Furthermore, this force is calculated using both the momentum forcing and the gravity terms in the solid solver. The purpose of this force is to lessen the acceleration of the motion of the deformable object towards the rigid surface. This repulsive force is applied only in the normal direction to the rigid walls and can be formulated as follows:

$$\mathbf{F}_c = k_w(-(\mathbf{F}_{ibm})_n - \mathbf{g}_n)(\frac{2h-d}{h}) \tag{10}$$

where K_w is a stiffness constant parameter used to control the strength of the collision force. The subscript n stands for the normal direction to the rigid surface. The term d stands for the shortest normal distance between the Lagrangian point of the flexible object and the closest solid wall boundary face center. The collision force is applied only if it is pointing towards the fluid domain.

3 Solution procedure

The overall solution procedure for the simulation of fluid-flexible structure interaction is summarized as follows:

- At the nth time step, the Lagrangian momentum forcing is calculated using the fluid flow velocity of the previous time step. Then, the Eulerian Momentum forcing is updated.
- Navier Stokes equations are solved to update both the fluid velocity field (u^{n+1}) and the pressure field (p^{n+1}).
- The new IB points (X_{ib}^{n+1}) are updated and then the Lagrangian momentum forcing is calculated.
- The equation of motion for the flexible objects is solved to update the solid position (X^{n+1}).

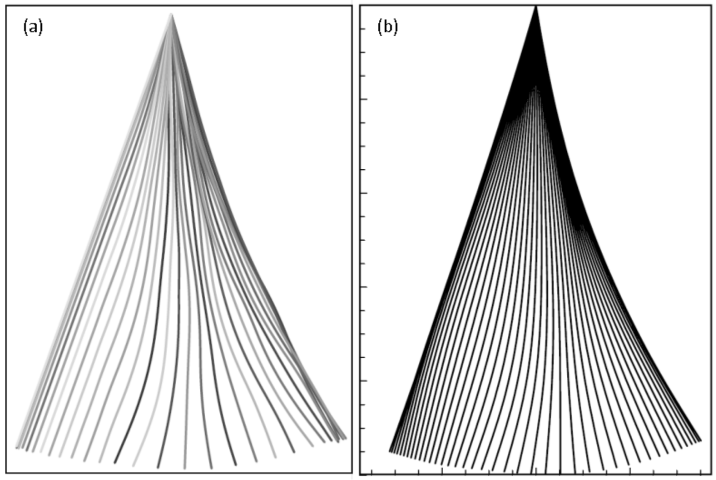

Figure 2: Superposition of the filament positions at successive times for a half cycle of the filament oscillation. Left: Present data, Right: data from Huang et. al, 2007 [23].

4 Results and Discussion

The present numerical method is applied to different fluid-structure interaction problems: A hanging filament without ambient fluid, a flow around a flexible filament fixed from one side and free from the other side, a flag oscillation in a free stream, a flag motion in a free stream and behind an obstacle, and a flag collision against a side wall and an obstacle. For the first problems, the model is validated against benchmarking data available in the literature. Then, the model is used for investigating the flag behavior in a free motion and under the different collision models proposed.

4.1 Two dimensional flexible filament in a free stream

To validate the present equation of motion for flexible objects, the motion of a hanging filament is investigated under the effect of the gravitational force and without ambient fluid. Therefore, the momentum forcing term in the solid solver is omitted in this case. The filament is fixed from one end and free from the other end. It has a length of $L = 1$ and a non dimensional bending rigidity $K_B = 0.01$. The initial position of the filament is inclined at an angle of 0.1π with the equilibrium. The only external force applied to the filament is the gravitational acceleration ($Fr = 10$). The filament is discretized using 64 points in the Lagrangian domain. Figure 2 shows a comparison of the filament superposition over successive time steps against the data presented by Huang et. al, 2007 [23]. During the oscillation, the filament behavior is analogous to a pendulum rope with a slightly curved line. The time history of the Y position for the filament's free end point (point A in Figure 1) is plotted in Figure 3. It is clear that the results obtained with the present solid solver agree very well with the previous studies in the literature. The equation of motion for the flexible object is solved considering that the filament does not extend during its motion (inextensibility condition). This is achieved by using a sufficiently large value for the tension coefficient. For $K_T = 1000$ in the previous test case, the error in the filament length is calculated at the time when the filament experiences a maximum deflection ($t = 1.38$) and is found to be equal to 0.23%. This proves that the filament satisfies the inextensibility condition during its oscillation.

The fluid - structure interaction coupling is validated using a flexible filament under the effect of a free stream. The filament has a length L and is pinned at the leading edge and free at the trailing edge. Both the free stream and the gravitational acceleration directions are parallel to the x-direction. The filament is initially inclined with respect to the free stream direction (the inclination angle with the x-direction is $\theta = 0.1\pi$). The size of the Eulerian computational domain is $[-2L, 6L] \times [-4L, 4L]$ and the Eulerian mesh step size in both the streamwise and transverse directions is $\Delta x = \Delta y = L/64$. The Dirichlet boundary condition is applied at the inflow with a velocity applied only in the x-direction ($u_x = U, u_y = 0$). A

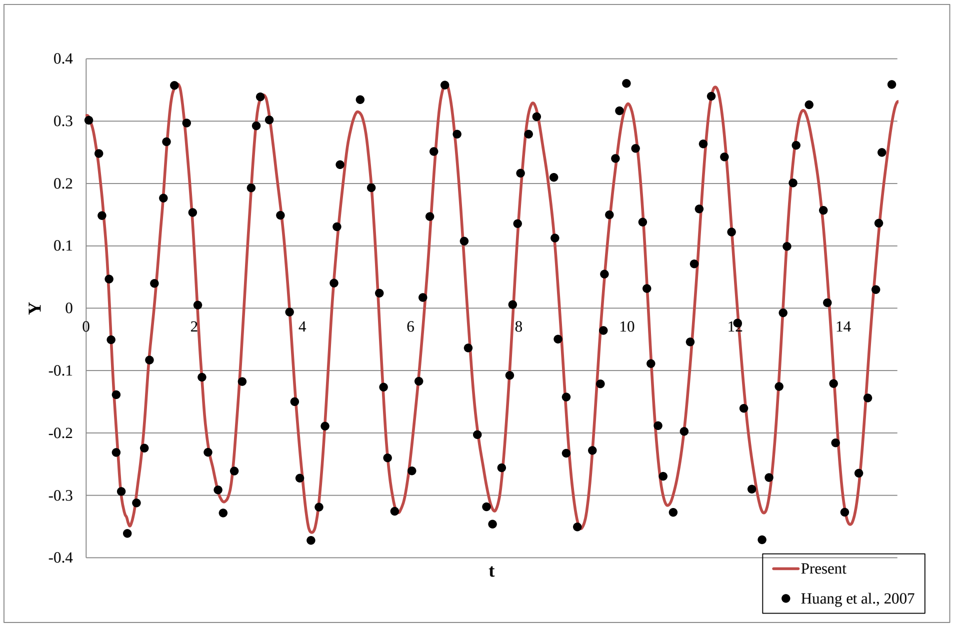

Figure 3: Time history of the free end position of the filament. The continuous line is the present results and the black dots are the data of Huang et. al, 2007 [23].

constant pressure boundary condition is applied at the outflow and a no-slip wall boundary condition is applied at the top and bottom sides of the numerical domain. The properties of the flexible filament and the characteristics of the numerical domain are described by the following dimensionless parameters: $\rho = 1.5$, $Fr = 0.5$, $Re = 200$, $K_B = 0.001$, $K_T = 1000$, and $\Delta s = L/64$. For filament oscillation under different Lagrangian mesh resolutions, Huang et al., 2007 [23] found a slight deviation in the results for Lagrangian mesh step sizes larger than $L/48$. Hence, the mesh resolution used in this work is considered to satisfy the mesh convergence criterion.

Figure 4 displays the time history of the trailing edge transverse location during the filament motion along with the results of Huang et. al, 2007 [23]. Two different cases are considered in our simulations: (i) $K_{ibm} = 10^5, \Delta t = 3 \times 10^{-4}$ and (ii) $K_{ibm} = 10^6, \Delta t = 1 \times 10^{-4}$. The instantaneous evolution of the trailing edge position highlights that the filament, under the prescribed conditions, develops a sustained flapping oscillation due to the coupled fluid - solid interaction. It is evidenced that the present results agree well with those from Huang et. al, 2007 [23]. However, a slight deviation is noticed in terms of the period of oscillation (case (ii)) and amplitude of oscillation (case (i)). The sensitivity of the numerical results to the choice of the constant (K_{ibm}) and the difference with the benchmarking data can be attributed to different reasons. The physical problem studied here is an unstable test case where the filament should experience a continuous oscillation due to the strong coupling between the fluid and the solid. Lee and Choi, 2015 have shown that for $\rho > 5$, the filament should experience unstable oscillations based on the value of the bending rigidity. In contrast, for density ratios $\rho < 5$, the filament oscillations due to external perturbations should dampen after a short period of time. For the industrial application of cloth transport through a pump, the cloth has density value close to that of the surrounding fluid and therefore the cloth, if fixed from one side, will come to rest after a short period of time. The benchmarking numerical data presented in Figure 4 are also obtained using different formulation for the momentum forcing with two large negative constants instead of the K_{ibm} employed in this paper. Figure 4 also highlights the sensitivity of the results to the choice of the time step size. This sensitivity is shown in Huang et. al, 2010 [11] when they derived the momentum forcing

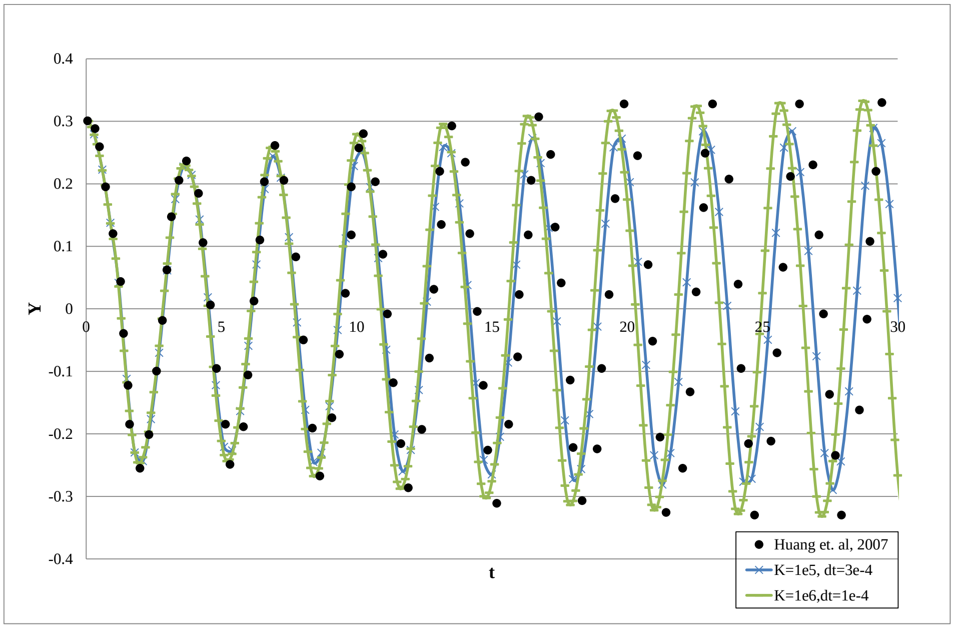

Figure 4: Time history of the transverse displacement of the free end position of the filament under the effect of both the fluid flow and gravity (Re=200, Fr=0.5). The continuous lines represent the current results and the black dots are provided by Huang et. al, 2007 [23].

formulation from the equation of motion of the flexible object. The authors suggest that the momentum forcing should be inversely proportional to the time step size. Thus, using higher values of K_{ibm} in the numerical simulations requires a reduction in the time step size in order to obtain consistent results and to avoid numerical instability. Numerical tests indicate that the constant K_{ibm} must be sufficiently large enough to couple the fluid and solid solvers. The choice of this IBM constant , however, is fairly arbitrary and depends on the type of flow and the physical problem considered.

Figure 5 shows the trajectory of the trailing edge for one single period (case ii) compared against the trajectory obtained by Lee and Choi, 2015 [12]. The numerical results in this paper display the figure of eight (∞) similarly to the literature. However, the results shown in [12] indicate a higher stretching of the filament in the transverse direction compared to the present results. The magnitude of the oscillation of the trailing edge obtained by Lee and Choi, 2015 [12] is also slightly higher than both the current results and the data of Huang et al, 2007 [23]. Figure 6 shows the vorticity contours at $Re = 200$ shed from the flexible filament during its oscillation for one complete period. This figure clearly shows the successive shedding of two small vortices combined into a single rotating structure. Similar conclusions also noticed by Huang et. al, 2007 [23] in terms of the behavior of the vortices behind the filament.

4.2 Three dimensional flapping flag in a free stream

In this section, a simulation of a 2D flag flapping in a three-dimensional flow is conducted. The schematic diagram of the flag inside the fluid domain with both Lagrangian and Eulerian coordinate systems is shown in Figure 1. The flag shape is square with length L and initial position inclined at an angle 0.1π from the x-direction. The plane xz is parallel to the streamwise direction and the y-axis is perpendicular to the free stream. The size of the computational domain is $[-L, 4L] \times [-2L, 2L] \times [-L, L]$. The fluid domain is discretized using a uniform mesh with mesh step size $\Delta x = \Delta y = \Delta z = L/25$. The mesh resolution used for

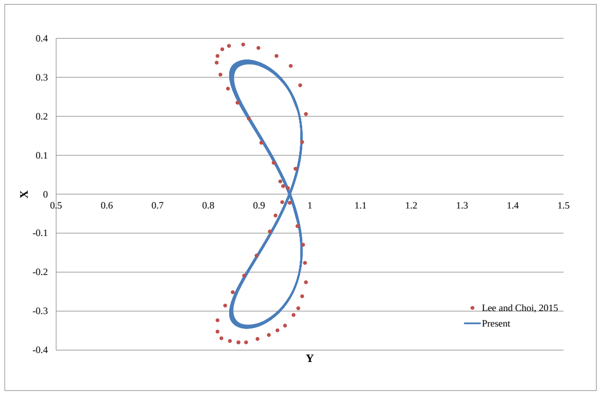

Figure 5: Trajectory of the trailing edge location during one full cycle of the filament oscillation compared to the results of Lee and Choi, 2015 [12].

the Lagrangian domain is $\Delta s_1 = \Delta s_2 = L/50$. The flag is fixed (pinned) from one end and free from the other ends so that the flapping under the effect of the fluid flow will be parallel to the y-direction. The Dirichlet boundary condition is applied at the inflow with a velocity applied only in the x-direction ($u_x = U, u_y = 0$). A constant pressure boundary condition is applied at the outflow and a no-slip wall boundary condition is applied at the top and bottom sides of the numerical domain. The properties of the flexible flag are described by the following non dimensional parameters. The density ratio $\rho = 1$, the tension coefficient and the bending rigidity in all the directions are $K_T = 100, K_B = 0.0001$, respectively. For comparison against the results of Huang et. al, 2010 [11], both Reynolds number and Froude number are chosen as: $Re = 200$ and $Fr = 0.0$, respectively. The momentum forcing is calculated using the IBM constant value $K_{ibm} = 10^5$ and the time step size considered in the simulations is $\Delta t = 3 \times 10^{-4}$. Later, the effect of the gravity will be activated to study the free flag motion in a free stream.

The instantaneous flag position at four different time instants is shown in Figure 7. During the flag oscillations, the trailing edge travels from its maximum transverse position across the equilibrium state (parallel to the xz plane) towards its maximum transverse position in the opposite side of the equilibrium plane and then it repeats the cycle again with sustained continuous oscillation. The flag during its motion has a symmetric shape in the spanwise direction as evidenced in [11]. Figure 8 shows the superposition of center line of the flag along with those obtained in Huang et. al, 2010 [11]. The center line as drawn in Figure 1 passes from the point A at the trailing edge parallel to the x-axis towards the leading edge of the flag. The behavior obtained in this paper for the center line during the oscillation is qualitatively comparable with those in Huang et. al, 2010 [11]. The figure of eight (∞) formed by the motion of the point A at the trailing edge can also be seen in this figure.

Figure 9 shows the time history of the trailing edge transverse location at the point A (as indicated in Figure 1) compared with the results of Huang et. al, 2010 [11]. The non dimensional time used in this figure is divided by the period of oscillation for the flag. The present results agree well with those in the literature. The flag undergoes sustained continues oscillations due to the coupled fluid - solid interaction. Furthermore, for $Re = 200$ the amplitude of oscillation of the sides of the trailing edge are the same as the center point A. Similar behavior is also noticed in the literature. There are, however, some discrepancies in both the phase and amplitude of oscillations. The percentage error in the magnitude (measured from peak to peak) compared to the literature is 3.4%. Figure 10 shows a snapshot of the vortical structure behind the flag where the hairpin-like vortices with two antennae are formed and shed from the flag after each flapping and it is shown to be approximately symmetrical about the flag center line. This flow pattern and the vortical structure around the flag is consistent with those observed by both Huang et. al, 2010 [11] and Lee and Choi, 2015 [12].

The discrepancies in the quantitative values for both phase and amplitude of oscillation are most likely

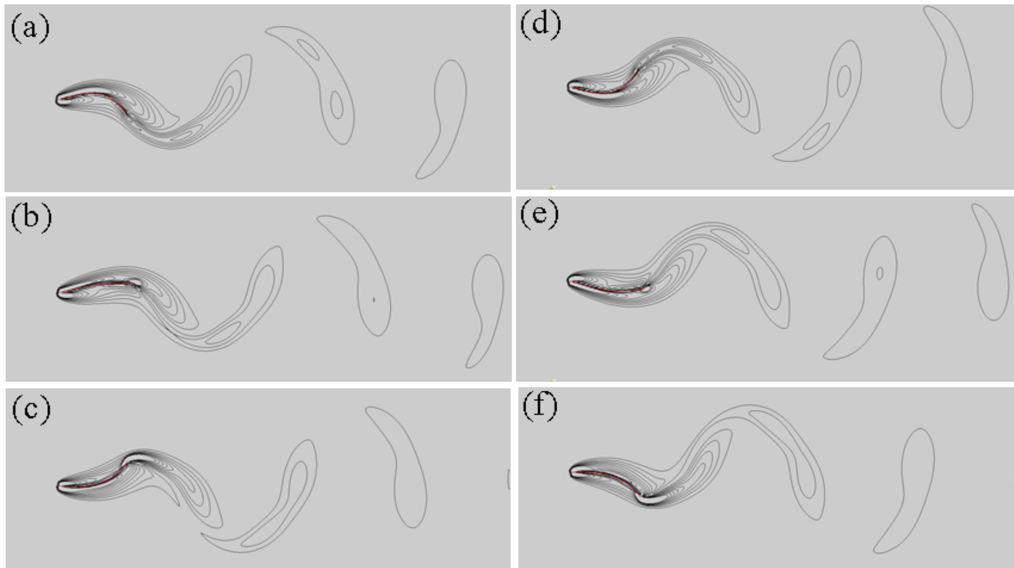

Figure 6: Instantaneous vorticity contour of a uniform flow over a filament at Re=200, Fr=0.5, $K_B = 0.001$, and $\rho = 1.5$. The non dimensional time sequence is as follows: (a) 20, (b) 20.25, (c) 20.5, (d) 20.75, (e) 21, (f) 21.25.

due to three main factors. First, despite the fact that the solid solver is discretized and solved using similar methods as applied in Huang et al., 2010 [11], the Navier Stokes equations (fluid domain) are solved using the PIMPLE solver in OpenFOAM while the projection method is used in Huang et. al, 2010 [11], and small difference in the flow solver can be expected to impact on the coupling in a non negligible way due to the highly dynamic nature of motion. Second, the value for the tension coefficient in the longitudinal direction used in this work is $K_T = 100$ which is one order less than the one used in Huang et. al, 2010 [11]. However, for stability reasons, smaller time step sizes are required in order to use larger values for the tension coefficient. Third, the numerical domain in the longitudinal direction is smaller than that in Huang et. al, 2010 [11]. The choice of the numerical domain was restricted due to computational limitations. This flag oscillation test case required large computational time in order to investigate the continuous sustained oscillations. Nevertheless, the present code was capable of predicting the sustained flag oscillations and flow structure consistent with published results in the literature. Results indicate that for flexible objects with large surface deformations, large tension coefficients should be used to satisfy the inextensibility condition. Also, the number of Lagrangian points required to capture properly the flag deformation and bending forces on the flag was also found to increase when the flag is expected to undergo large surface deformations. The IBM constant should also be chosen a priori based on both theoretical and experimental understanding of the problem under investigation.

4.3 Three dimensional free flag motion

In this section, the effect of the solid to fluid density ratio ρ on the behavior of a free moving flag in a uniform flow is studied. The size of the computational domain is $[-L, 7L] \times [-L, L] \times [-L, L]$. The Eulerian domain is discretized using a uniform structured mesh with mesh size $\Delta x = \Delta y = \Delta z = L/25$. The flag is initially positioned parallel to the yz plane at a distance $x = L$ from the inlet boundary condition. The initial shape of the flag is square with side length L. The number of points representing the Lagrangian domain are 50×50. The free boundary condition is applied at all the sides of the flexible flag so that it moves freely under the effect of the fluid flow. The Dirichlet boundary condition is considered at the inflow with a non-zero velocity applied only in the x-direction ($u_x = U, u_y = 0$). A constant pressure boundary condition is applied at the outflow and a no-slip wall boundary condition is applied at the top and bottom sides of the numerical domain. In the present simulations, we use $Re = 200$ and $Fr = 10$ for the fluid domain, and

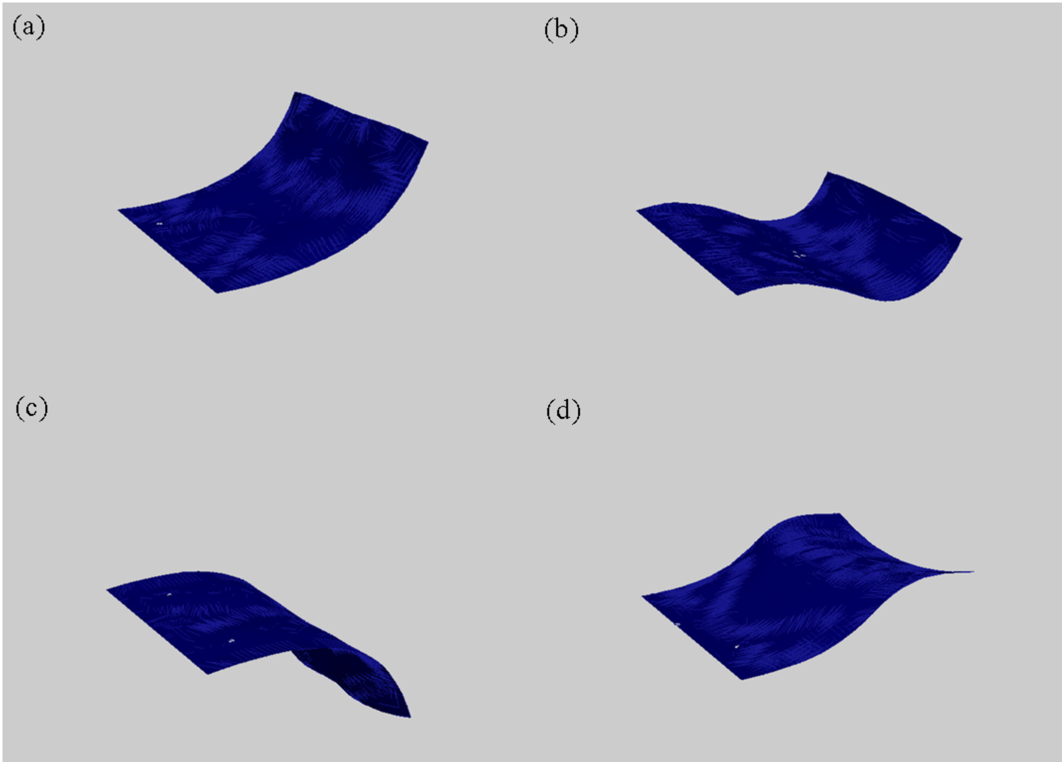

Figure 7: Instantaneous positions of a flapping flag at four instants labelled as:(a):5.4, (b):6.3, (c):7.2, (d):8.1.

$K_T = 100$ and $K_B = 0.001$ for the elastic surface. The gravitational acceleration is applied along with the free stream direction (x- direction). Four different values for the solid - fluid density ratios are considered $\rho = 0.05, 0.5, 1$ and 2. The IBM constant used in calculating the Lagrangian momentum forcing term is set to $K_{ibm} = 10^5$, and a time step size of $\Delta t = 3 \times 10^{-4}$ is used.

Figure 11 displays snapshots of the flag under successive time steps during its motion in the free stream direction (x - direction) for the four density ratios considered. For each test case, the flag is visualized starting from its initial position (left side of the figure) until it leaves the numerical domain. The step size between the successive images is constant for all the density ratios ($t = 0.3$). The time required for the flag to travel along the fluid domain varies from $t = 1.7$ for $\rho = 2$ to $t = 3.8$ for $\rho = 0.05$ indicating that the flag travels faster for the large density ratios. For all the test cases, the flag deforms slightly during its motion taking a concave shape for the small density ratios. The shape of the flag is more flattened for the large density ratios. Furthermore, the flag with the small density ratios sustains its deformed shape during the motion. In contrast, for large density ratios, the flag deforms and recovers its flat shape while flowing along with the free stream. Apart from the speed of the flag during its motion, all the studied cases proves that the the flag retains its symmetric shape during the motion in the uniform flow. To investigate the effect of a non-uniform fluid flow on the motion of flexible objects, the flag with density ratio $\rho = 0.05$ is located in the entrainment region behind an obstacle with a square shape. The numerical domain used in the free flag motion is considered. In addition, and obstacle with a dimension of $0.4L \times 0.4L \times 2L$ is positioned at location $x = 0$. The top image in Figure 12 shows the obstacle inside the fluid domain and the initial position of the flag behind the obstacle. The numerical simulation is performed first without considering the flag inside the numerical domain in order to provide a sufficient time to develop the wake behind the obstacle (Time considered for the fluid solver only is $t = 0.9$). The flag is then positioned in the wake region at a distance $x = L$. Figure 12 shows that the flag experiences large deformations compared to the one located in a free stream. Based on the deformation of the flag, three different regions can be noticed; the sides of the flag which are exposed directly to the free stream and the center of the flag which is positioned in the wake region behind the obstacle. The flag travels faster at its sides than the center. As a consequence,

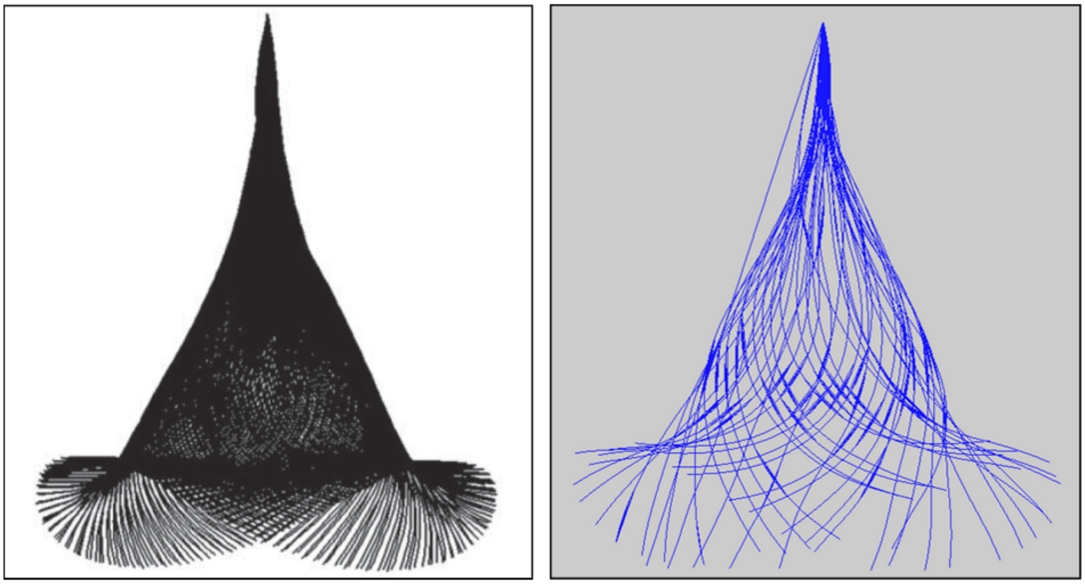

Figure 8: Top view of superposition of the flag's center line passing through the point A at the trailing edge. Right: present data, Left: data from Huang et. al, 2010[11].

the flag is exposed to strong deformations so that it loses its symmetrical shape in the downstream flow. Thus, for fluid structure interaction problems in waste water pumps with flexible objects having slightly larger densities than the surrounding fluid, the flow pattern plays a significant role in the behavior of the rag during its motion inside the pump. Large vortical structures and non-uniform flows enhance the large deformation of the flexible bodies which, in turn, increases the possibility of rag clogging in the trailing edge of the impeller of waste water pumps. Hence, reducing the efficiency of the pump. For extensible clogged rags inside the pump, a maintenance procedure is required to clean the pump so it returns to its standard operational condition.

4.4 Flag collision against rigid objects

In this section the collision models implemented in the numerical code are studied. First, the free motion and collision of a flexible flag against the side walls of the fluid domain is considered. The size of the computational domain is $[-L, 7L] \times [-L, L] \times [-L, L]$. The fluid domain is discretized using a uniform structured mesh with mesh size $\Delta x = \Delta y = \Delta z = L/25$. The flag has a square initial shape with side length L and is initially positioned parallel to the xz plane at a height $y = 0.5L$ from the lower wall of the fluid region (See the top image in Figure 13). The number of points representing the Lagrangian domain are 50×50. The free boundary condition is applied at all the sides of the flexible flag so that it moves freely under the effect of the fluid flow. The Dirichlet boundary condition is considered at the inflow with a non-zero velocity applied only in the x-direction ($u_x = U, u_y = 0$). In the present simulations, we use $Re = 200$ and $Fr = 0.5$ for the fluid domain, and $K_T = 100$ and $K_B = 0.001$ for the elastic surface. The gravitational acceleration is applied at an angle $\theta = -45°$ with the free stream direction (x- direction). Two different values of the solid - fluid density ratio are considered $\rho = 0.5$ and 1. For each density ratio, two values for the collision stiffness constant are studied $K_w = 0.1$ and 1. The IBM constant used in calculating the Lagrangian momentum forcing term is set to $K_{ibm} = 10^5$ and a time step size of $\Delta t = 3 \times 10^{-4}$ is used.

Figure 13 shows the visualization of the flag during it motion and collision against the bottom wall of the fluid domain for the repulsive collision force model with $\rho = 0.5$ and $K_w = 0.1$. Due to the effect of the fluid flow, the flag travels along the x-direction. However, the flag transforms also in y-direction and gets closer to the bottom wall due to the effect of the gravity. The flag does not sustain its horizontal shape. Rather, a deformation in the flag is noticed. This shape deformation strengthens once the flag's leading edge starts penetrating the region of the boundary layer. During the approach, the flag does not collide against

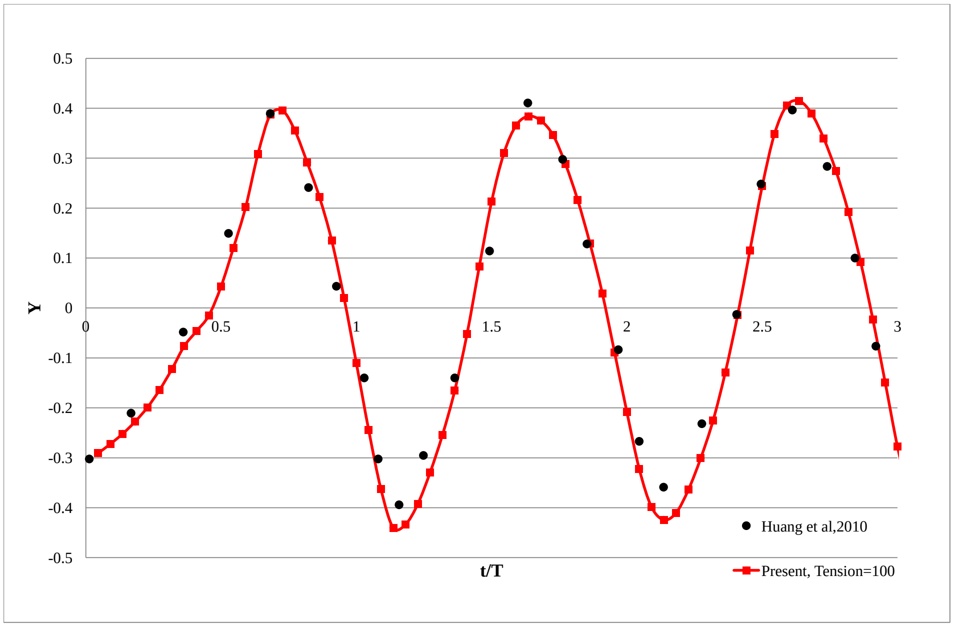

Figure 9: Time history of the transverse displacement of the point A at center of the trailing edge of the flag for Re=200 and Fr=0.0. The continuous line is for the present data and the black dots are for the data of Huang et. al, 2010[11].

the rigid wall and a thin liquid film is maintained separating the flexible and rigid surfaces. Following the initial approach phase, the flag starts rebounding from the solid surface and the minimum film thickness shifts from the leading edge towards the trailing edge. Then, the flag travels parallel to the bottom wall creating a conical liquid film with the solid surface. The conical shape has its large radius at the leading edge of the flag and its small radius at the trailing edge.

Figure 14 plots the history of motion for the flag center line (as indicated in Figure 1) for the different density ratios and collision constants mentioned above. It is clear that the collision of the flag is strongly influenced by the solid fluid density ratio. For $\rho = 1$, the thickness of the film trapped between the two solid surfaces is thinner than the case with $\rho = 0.5$. However, the liquid film is always maintained between the solid domains. This indicates that neutrally buoyant flag approaching a rigid wall inside a fluid domain would not rebound or collide with the rigid surface. Instead, the flag will slide along the rigid surface with a thin liquid film remaining between the two solid domains. Figure 14 also highlights that for large density ratios, there is a strong sensitivity of the numerical results to the choice of the collision constant K_w. For $\rho = 1$, higher values for K_w are required in order to avoid the penetration. The dependence of the collision process on the value of the constant K_w decreases for smaller solid to fluid density ratios. More in depth studies for the collision constant K_w and the collision force will be discussed in future works.

The hard sphere like collision model is also applied to the flag collision problem described above (The results are not shown here). The Lagrangian points are flagged once their normal distance to the rigid surface falls below $2h$. The hard sphere model applied in this code advances the flagged Lagrangian points using only the velocity of the fluid domain. This prevents the penetration of the flexible object inside the rigid wall as the value of the velocity component normal to the wall at the boundary cells is zero. Due to the existence of the boundary layer, the flagged Lagrangian points in this layer are advanced in the flow direction using very small velocity values compared to the points away from the boundary layer. This leads to large stretching of the flag in the flow direction as the points close to the wall are almost pinned to the wall

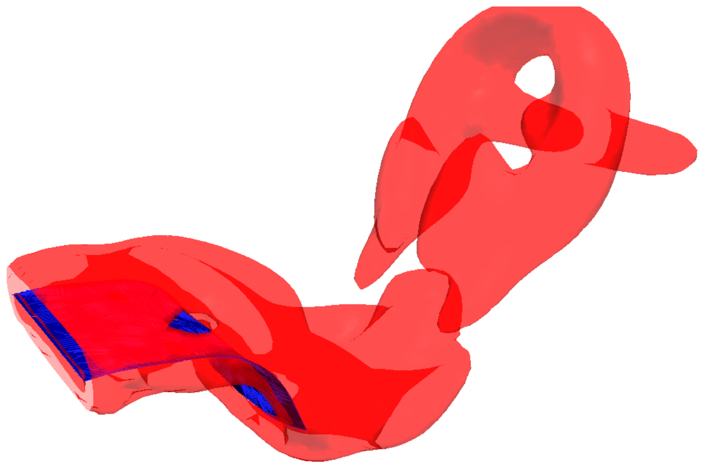

Figure 10: Vortical structures shedding from the flapping flag at the instant when the trailing edge reaches its minimum transverse position.

while the rest of the flag points are advancing in consistent with the free stream. Thus, applying the hard sphere like collision model violates the inextensibility condition applied in this code which, in turn, leads to numerical instability. The comparison of the efficiency and accuracy of both collision models implemented highlights the superiority of the repulsive force collision model for simulating the interaction between the flexible object and the rigid wall. Furthermore, contrary to the hard sphere model, the repulsive force takes into account the effect of the fluid flow in the region around the flag and inside the film region similarly to the lubrication models.

The repulsive force collision model is implemented for the simulation of flag collision against a bluff rigid body with rectangular shape ($L \times 0.4L$). The numerical fluid domain is similar to the one used for the collision analysis above. The fluid domain is defined using $Re = 200$ and $Fr = 0.5$. The gravitational acceleration and the fluid flow are parallel to the x-direction. The density ratio employed in this case is very close to the neutrally buoyant case ($\rho = 0.05$) and the collision force is calculated using the constant $K_w = 0.1$. The obstacle is positioned at $x = 2L$. The initial shape of the flag is parallel to the yz plane and located at $x = L$. The sides of the flag are closer to the upper wall than the lower wall. This position is chosen so that the flag does not get caught with the obstacle (This will be performed in future work). Figure 15 shows the visualization of the flag during its motion and collision against the obstacle. The background in this figure depicts the flow velocity pattern and the wake generated behind the obstacle. As the flag gets closer to the obstacle, the lower side of the flag collides against the obstacle while the upper part continues moving with the free stream. This leads to large surface deformation around the top left corner of the obstacle. Afterwards, the flag continues deforming and wraps around the obstacle. However, the flag does not wrap completely around the corner of the obstacle due to the bending rigidity of the flag. Then, the trailing edge of the flag rebounds from the side edge of the obstacle and the flag recovers its straight shape as it moves in the downstream direction. The restoring of the flat shape occurs only at the trailing edge which moves faster than the leading edge. The surface starts deforming again as the flag moves behind the obstacle and gets entrained into the wake region of the obstacle. Depending on the inertia of the fluid flow and the solid bending rigidity, the flag might deform strongly and experience a self collision. Further analysis of the collision against solid obstacles will be performed in future works.

5 Conclusions and Future Work

In the present study, an immersed boundary method has been implemented and validated for the study of fluid structure interaction problems. The equation of motion for the deformable object is solved on a Lagrangian grid using the Finite Difference method, while the Navier Stokes equations for modeling the fluid domain are solved on an Eulerian grid using the PIMPLE solver available in the open source library

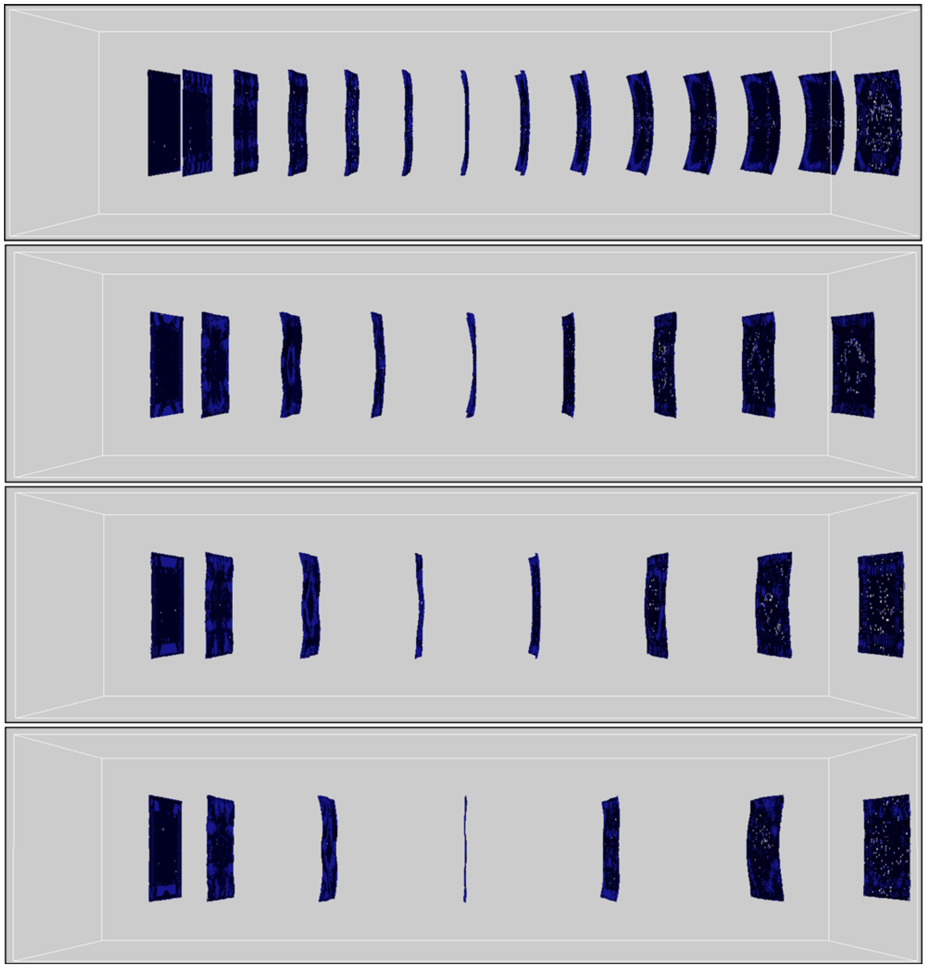

Figure 11: Superposition of the flag positions at different time intervals (t=0.3) during its free motion for four different solid fluid density ratios ordered from top to bottom as: $\rho = 0.05, 0.5, 1,$ and 2, respectively.

(OpenFOAM-2.3.1). A momentum forcing term is added to the solid equation in order to account for the fluid structure interaction. This force is spread into the Eulerian domain using smoothed Dirac function. The numerical model is validated first using two different test cases: (i) filament flapping in a free stream, and (ii) three dimensional flag flapping in a free stream. Despite the instability of the problems considered due to the sustained continuous oscillation of the filament/flag and the large solid fluid density ratio, the results were comparable to those available in the literature. The present data, however, showed the strong sensitivity of the results to the choice of the constant K_{ibm} and the time step size in the numerical model.

The model is then extended for the study of the free flag/rag motion inside a fluid domain. The results highlighted the influence of the flow pattern on the behavior of the flag during its travel in the downstream direction. This was evidenced by the symmetrical motion of the flag in a free stream while large deformations are observed when the flag moves in the wake region of an obstacle.

Two different collision models are considered in this work: a hard sphere like collision model and a repulsive force collision model. The two methods are implemented for the study of flag collision against the side walls of the numerical domain and the results highlighted the importance of using a force like model to avoid the penetration of the deformable object into the rigid wall. This collision force should take into account the forces acting on the flag in the film region between the rigid and deformable solid objects. Early experimental results performed in an in-house water tunnel supports the observations noticed with the force collision model for rag collision against the side walls of the water tunnel. For future works, the numerical results for the free rag motion and collision will be compared against experimental data. The collision

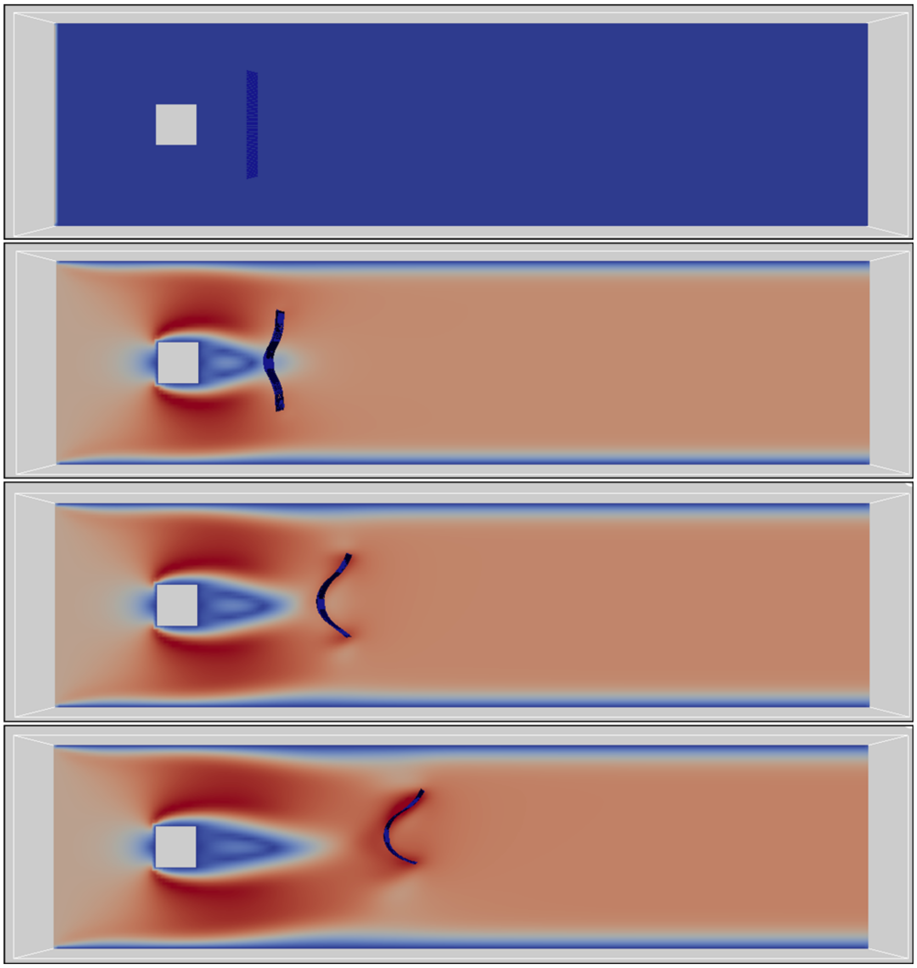

Figure 12: Instantaneous positions of the free moving flag behind an obstacle at four different instants labeled from top to bottom as: 0, 1.26, 1.62, and 1.98.

model will also be extended to consider both the lubrication and the friction effects in the film region. More complicated test cases analogous to what is happening inside waste water pumps will also be considered. To conclude, the present results in this work have provided an initial work towards the study of rag motion and clogging inside waste water pumps.

6 Acknowledgment

The present research is funded by Enterprise Ireland and Sulzer Pump Solutions Ireland under the Innovation Partnership Programme (Grant No. IP/2014/0359).

References

[1] Wei-Xi Huang and Hyung Jin Sung. An immersed boundary method for fluid flexible structure interaction. *Computer Methods in Applied Mechanics and Engineering*, 198(33):2650–2661, 2009.

[2] Roland Glowinski, T-W Pan, Todd I. Hesla, and Daniel D. Joseph. A distributed lagrange multiplier/fictitious domain method for particulate flows. *International Journal of Multiphase Flow*, 25(5):755–794, 1999.

[3] Fang-Bao Tian, Hu Dai, Haoxiang Luo, James F. Doyle, and Bernard Rousseau. Fluid structure

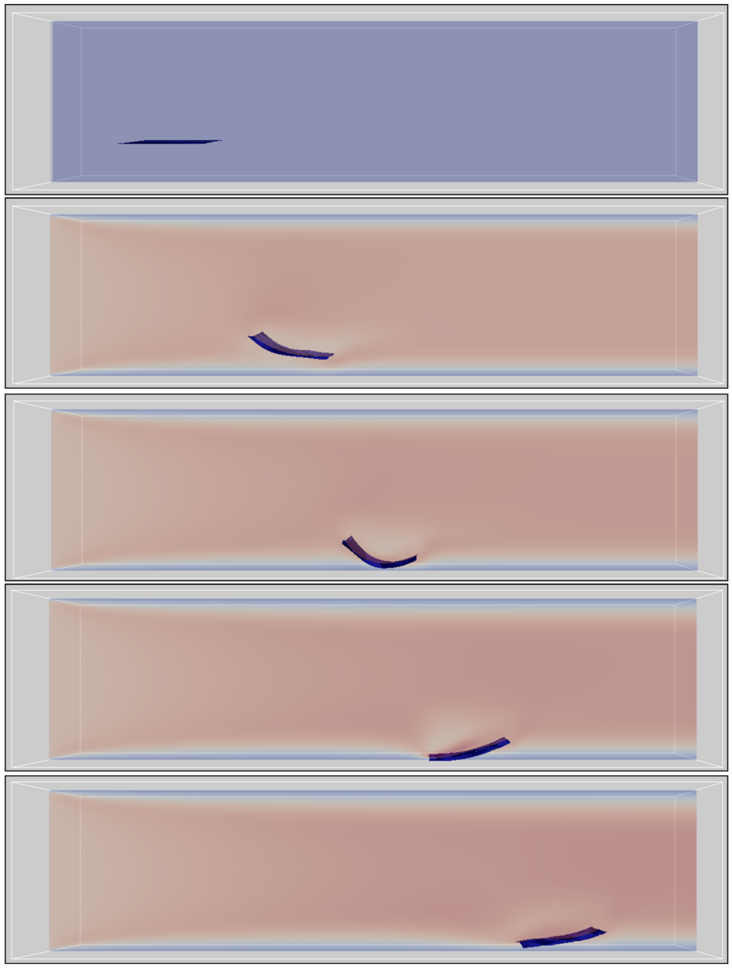

Figure 13: Instantaneous positions of the free moving flag colliding against the bottom wall of the numerical domain at five different instants labeled from top to bottom as: 0, 2.1, 3, 3.9, and 4.8. $\rho = 0.5$ and $K_w = 0.1$.

interaction involving large deformations: 3d simulations and applications to biological systems. *Journal of computational physics*, 258:451–469, 2014.

[4] TT Nguyen, Dhanabalan Shyam Sundar, Khoon Seng Yeo, and Tee Tai Lim. Modeling and analysis of insect-like flexible wings at low reynolds number. *Journal of Fluids and Structures*, 62:294–317, 2016.

[5] Yi Sui, Yong Tian Chew, Partha Roy, and Hong Tong Low. A hybrid immersed boundary and multi block lattice boltzmann method for simulating fluid and moving boundaries interactions. *International Journal for Numerical Methods in Fluids*, 53(11):1727–1754, 2007.

[6] Michel Bergmann and Angelo Iollo. Modeling and simulation of fish-like swimming. *Journal of Computational Physics*, 230(2):329–348, 2011.

[7] Hong-Bin Deng, Yuan-Qing Xu, Duan-Duan Chen, Hu Dai, Jian Wu, and Fang-Bao Tian. On numerical modeling of animal swimming and flight. *Computational Mechanics*, 52(6):1221–1242, 2013.

[8] Anvar Gilmanov, Trung Bao Le, and Fotis Sotiropoulos. A numerical approach for simulating fluid structure interaction of flexible thin shells undergoing arbitrarily large deformations in complex domains. *Journal of Computational Physics*, 300:814–843, 2015.

[9] Jihyun Bae, Jeongsu Lee, SeongMin Kim, Jaewook Ha, Byoung-Sun Lee, YoungJun Park, Chweelin Choong, Jin-Baek Kim, Zhong Lin Wang, and Ho-Young Kim. Flutter-driven triboelectrification for harvesting wind energy. *Nature Communications*, 5, 2014.

[10] Tomohiro Sawada and Toshiaki Hisada. Fluid structure interaction analysis of the two-dimensional flag-in-wind problem by an interface-tracking ale finite element method. *Computers & Fluids*, 36(1):136–146,

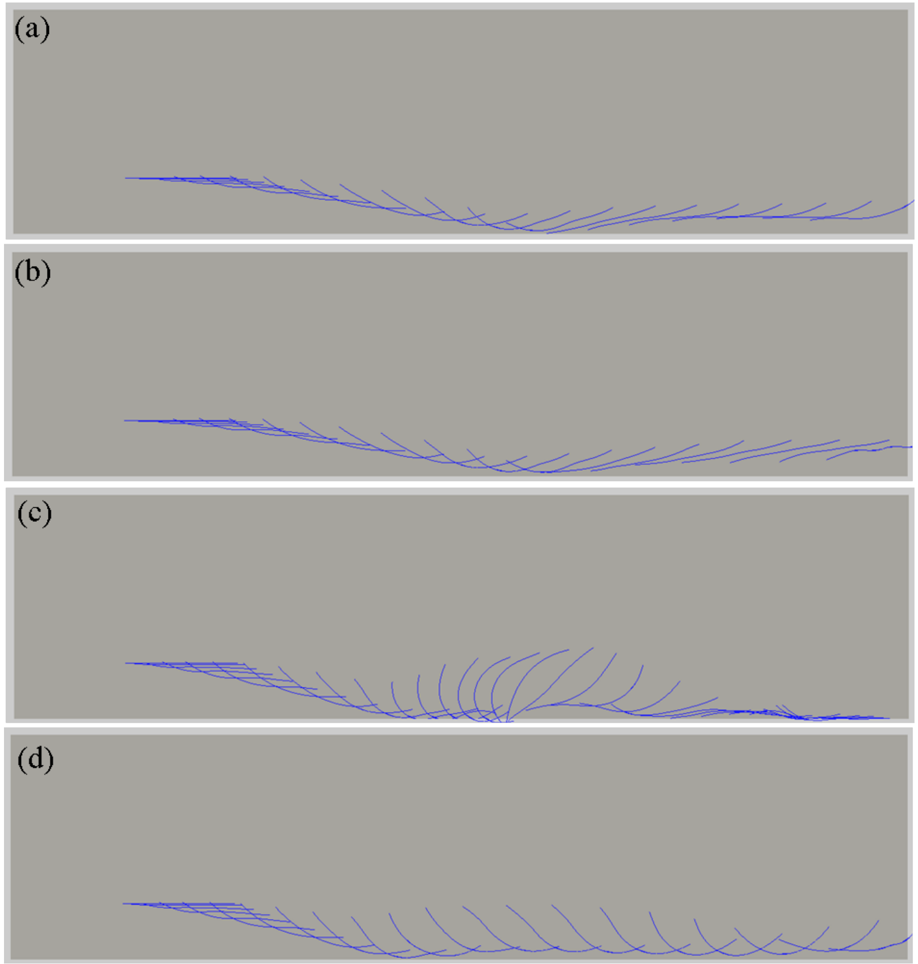

Figure 14: Front view of superposition of the flag's center line during its collision against the bottom side of the numerical domain. The four different cases are defined as: (a):$\rho = 0.5$ and $K_w = 0.1$, (b):$\rho = 0.5$ and $K_w = 1$, (c):$\rho = 1$ and $K_w = 0.1$, (d):$\rho = 1$ and $K_w = 1$.

2007.

[11] Wei-Xi Huang and Hyung Jin Sung. Three-dimensional simulation of a flapping flag in a uniform flow. *Journal of Fluid Mechanics*, 653:301–336, 2010.

[12] Injae Lee and Haecheon Choi. A discrete forcing immersed boundary method for the fluidâĂŞstructure interaction of an elastic slender body. *Journal of Computational Physics*, 280:529–546, 2015.

[13] Jaeha Ryu, Sung Goon Park, Boyoung Kim, and Hyung Jin Sung. Flapping dynamics of an inverted flag in a uniform flow. *Journal of Fluids and Structures*, 57:159–169, 2015.

[14] CW Hirt, Anthony A. Amsden, and JL Cook. An arbitrary lagrangian-eulerian computing method for all flow speeds. *Journal of Computational Physics*, 14(3):227–253, 1974.

[15] Jean Donea, S. Giuliani, and Jean-Pierre Halleux. An arbitrary lagrangian-eulerian finite element method for transient dynamic fluid-structure interactions. *Computer Methods in Applied Mechanics and Engineering*, 33(1-3):689–723, 1982.

[16] Charles Samuel Peskin. Flow patterns around heart valves: a digital computer method for solving the equations of motion, 1972.

[17] Yu-Heng Tseng and Joel H. Ferziger. A ghost-cell immersed boundary method for flow in complex geometry. *Journal of computational physics*, 192(2):593–623, 2003.

[18] Rajat Mittal, Haibo Dong, Meliha Bozkurttas, FM Najjar, Abel Vargas, and Alfred von Loebbecke. A versatile sharp interface immersed boundary method for incompressible flows with complex boundaries.

Journal of computational physics, 227(10):4825–4852, 2008.
[19] Kunihiko Taira and Tim Colonius. The immersed boundary method: a projection approach. *Journal of Computational Physics*, 225(2):2118–2137, 2007.
[20] EA Fadlun, R Verzicco, P Orlandi, and J. Mohd-Yusof. Combined immersed-boundary finite-difference methods for three-dimensional complex flow simulations. *Journal of Computational Physics*, 161(1):35–60, 2000.
[21] Jungwoo Kim, Dongjoo Kim, and Haecheon Choi. An immersed-boundary finite-volume method for simulations of flow in complex geometries. *Journal of Computational Physics*, 171(1):132–150, 2001.
[22] D. Goldstein, R. Handler, and L. Sirovich. Modeling a no-slip flow boundary with an external force field. *Journal of Computational Physics*, 105(2):354–366, 1993.
[23] Wei-Xi Huang, Soo Jai Shin, and Hyung Jin Sung. Simulation of flexible filaments in a uniform flow by the immersed boundary method. *Journal of Computational Physics*, 226(2):2206–2228, 2007.
[24] Fotis Sotiropoulos and Xiaolei Yang. Immersed boundary methods for simulating fluid structure interaction. *Progress in Aerospace Sciences*, 65:1–21, 2014.
[25] Rajat Mittal and Gianluca Iaccarino. Immersed boundary methods. *Annu.Rev.Fluid Mech.*, 37:239–261, 2005.
[26] Charles S. Peskin. Numerical analysis of blood flow in the heart. *Journal of computational physics*, 25(3):220–252, 1977.
[27] Yongsam Kim and Charles S. Peskin. Penalty immersed boundary method for an elastic boundary with mass. *Physics of Fluids (1994-present)*, 19(5):053103, 2007.
[28] Injae Lee and Haecheon Choi. A discrete forcing immersed boundary method for the fluidâĂŞstructure interaction of an elastic slender body. *Journal of Computational Physics*, 280:529–546, 2015.
[29] Dingyi Pan, Xueming Shao, Jian Deng, and Zhaosheng Yu. Simulations of passive oscillation of a flexible plate in the wake of a cylinder by immersed boundary method. *European Journal of Mechanics-B/Fluids*, 46:17–27, 2014.
[30] Benjamin SH Connell and Dick KP Yue. Flapping dynamics of a flag in a uniform stream. *Journal of Fluid Mechanics*, 581:33–67, 2007.
[31] Xiaojue Zhu, Guowei He, and Xing Zhang. An improved direct-forcing immersed boundary method for fluid-structure interaction simulations. *Journal of Fluids Engineering*, 136(4):040903, 2014.
[32] Fang-Bao Tian, Hu Dai, Haoxiang Luo, James F. Doyle, and Bernard Rousseau. Fluid structure interaction involving large deformations: 3d simulations and applications to biological systems. *Journal of computational physics*, 258:451–469, 2014.
[33] Fang-Bao Tian, Haoxiang Luo, Luoding Zhu, James C. Liao, and Xi-Yun Lu. An efficient immersed boundary-lattice boltzmann method for the hydrodynamic interaction of elastic filaments. *Journal of computational physics*, 230(19):7266–7283, 2011.
[34] Jinmo Lee and Donghyun You. Study of vortex-shedding-induced vibration of a flexible splitter plate behind a cylinder. *Physics of Fluids (1994-present)*, 25(11):110811, 2013.
[35] OpenFOAM Ltd. The open source computational fluid dynamics (cfd) toolbox, http://openfoam.com/, 2016.
[36] CFD Open. *OpenFOAM - 3.0.1 user guide*, 2015.
[37] Joel H. Ferziger and Milovan Peric. *Computational methods for fluid dynamics*. Springer Science & Business Media, 2012.
[38] RI Issa. Solution of the implicitly discretised fluid flow equations by operator-splitting. *Journal of Computational physics*, 62(1):40–65, 1986.
[39] Howard H. Hu, Neelesh A. Patankar, and MY Zhu. Direct numerical simulations of fluid solid systems using the arbitrary lagrangian eulerian technique. *Journal of Computational Physics*, 169(2):427–462, 2001.
[40] Samuel F. Foerster, Michel Y. Louge, Hongder Chang, and Khedidja Allia. Measurements of the collision properties of small spheres. *Physics of Fluids (1994-present)*, 6(3):1108–1115, 1994.
[41] Daoyin Liu, Changsheng Bu, and Xiaoping Chen. Development and test of cfd dem model for complex geometry: A coupling algorithm for fluent and dem. *Computers & Chemical Engineering*, 58:260–268, 2013.
[42] BH Xu and AB Yu. Numerical simulation of the gas-solid flow in a fluidized bed by combining discrete particle method with computational fluid dynamics. *Chemical Engineering Science*, 52(16):2785–2809,

1997.

[43] Decheng Wan and Stefan Turek. Direct numerical simulation of particulate flow via multigrid fem techniques and the fictitious boundary method. *International Journal for Numerical Methods in Fluids*, 51(5):531–566, 2006.

[44] Bertrand Maury. A many body lubrication model. *Comptes Rendus de l'Academie des Sciences-Series I-Mathematics*, 325(9):1053–1058, 1997.

[45] Tobias Kempe and Jochen Frohlich. Collision modelling for the interface resolved simulation of spherical particles in viscous fluids. *Journal of Fluid Mechanics*, 709:445–489, 2012.

[46] Abouelmagd Abdelsamie, Amir Eshghinejad Fard, Timo Oster, and Dominique Thevenin. Impact of the collision model for fully resolved particles interacting in a fluid. In *ASME 2014 4th Joint US-European Fluids Engineering Division Summer Meeting collocated with the ASME 2014 12th International Conference on Nanochannels, Microchannels, and Minichannels*, pages V01CT23A009–V01CT23A009. American Society of Mechanical Engineers, 2014.

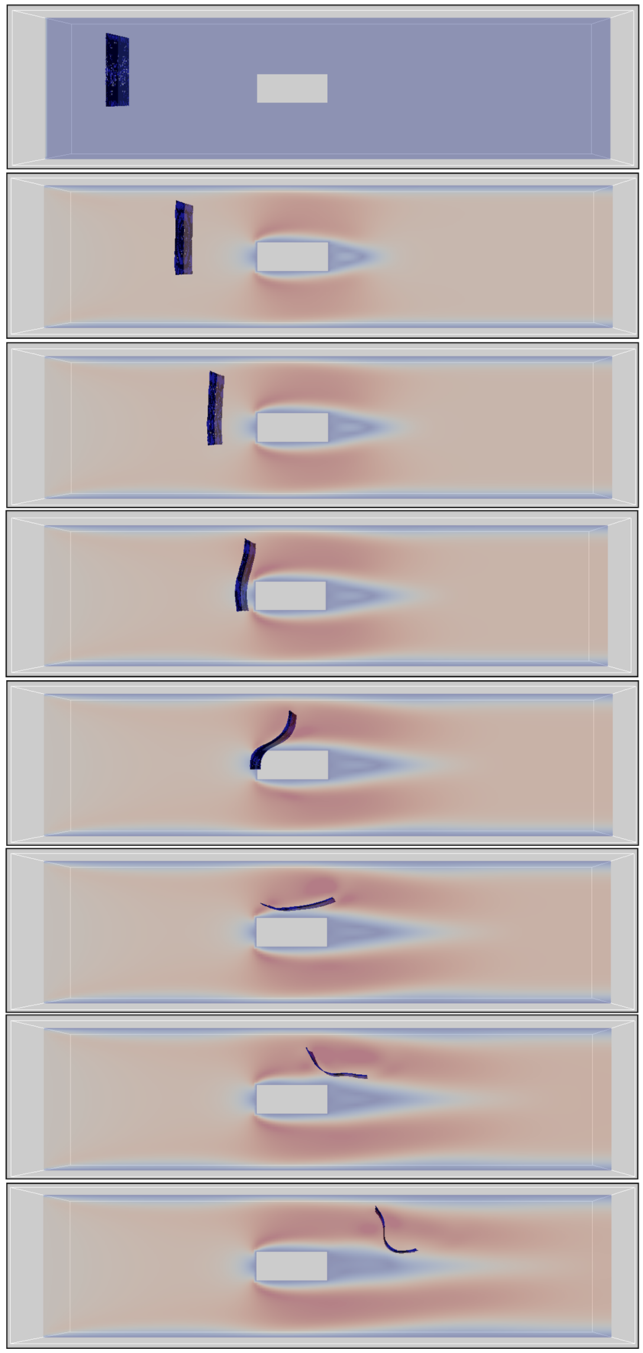

Figure 15: Instantaneous positions of the free moving flag passing through an obstacle inside the numerical domain at different instants labeled from top to bottom as: 0, 0.9, 1.26, 1.62, 1.98, 2.34, 2.7, and 3.24. $\rho = 0.05$ and $K_w = 0.1$.